Optical and Galvanomagnetic Properties of $\mathrm{Bi}_{1-x}\mathrm{Sb}_x$ Thin Films in the Terahertz Frequency Range

Anton D. Zaitsev [1,*], **Petr S. Demchenko** [1], **Dmitry V. Zykov** [1], **Ekaterina A. Korotina** [1], **Elena S. Makarova** [2], **Ivan L. Tkhorzhevskiy** [2], **Anastasiia S. Tukmakova** [2], **Natallya S. Kablukova** [3,4], **Aleksei V. Asach** [2] and **Anna V. Novotelnova** [2] and **Mikhail K. Khodzitsky** [1]

[1] Terahertz Biomedicine Laboratory, ITMO University, 197101 Saint-Petersburg, Russia; petr.s.demchenko@gmail.com (P.S.D.); dvzykov@itmo.ru (D.V.Z.); k.korotina28@gmail.com (E.A.K.); khodzitskiy@yandex.ru (M.K.K.)

[2] Faculty of Cryogenic Engineering, ITMO University, 197101 Saint-Petersburg, Russia; makarova_helena_2011@mail.ru (E.S.M.); tkhorzhevskiy.ivan.l@gmail.com (I.L.T.); astukmakova@itmo.ru (A.S.T.); avasach@itmo.ru (A.V.A.); novotelnova@itmo.ru (A.V.N.)

[3] International Scientific and Research Institute of Bioengineering, ITMO University, 197101 Saint-Petersburg, Russia; kablukova.natali@yandex.ru

[4] The Department of Physics, Saint Petersburg State University of Industrial Technologies and Design, 191186 Saint-Petersburg, Russia

[*] Correspondence: a.zaytsev@niuitmo.ru

Abstract: We report results of galvanomagnetic and terahertz time-domain spectroscopy measurements on thin films of $\mathrm{Bi}_{1-x}\mathrm{Sb}_x$ on polyimide and mica substrates with various antimony concentrations (x from 0 to 15 %) and film thickness (70, 150 nm). The resistivity, Hall coefficient and magnetoresistivity of the films were measured experimentally in the magnetic field of 0.65 T at room temperature. Mobility and concentration of electrons and holes in the film plane were calculated using the transport coefficients. The terahertz time-domain spectroscopy is used to measure the complex conductivity and permittivity of $\mathrm{Bi}_{1-x}\mathrm{Sb}_x$ thin films on the dielectric substrates in the frequency range from 0.2 to 1 THz. The plasma frequency, relaxation time, DC conductivity and effective carrier mass were extracted from these data and evaluated as functions of the Sb concentration for different film thickness and substrate. We observed that the film magnetoresistivity decreases with increasing the Sb concentration and for most of the films the Hall coefficient is negative and depends on the external factors insignificantly. We show that the mobility of charge carriers weakly depends on Sb concentration, which confirms the assertion about the scattering of carriers on themselves and not on defects in the structure. It was revealed that film static and dynamic resistivity (conductivity) as well as dielectric permittivity depend on Sb content and the film thickness. The results may be used for development of various thermoelectric, electronic and optical devices, such as THz detectors or components which can control the properties of THz radiation.

Keywords: semimetals; thin films; bismuth-antimony; galvanomagnetic properties; terahertz time-domain spectroscopy; solid solutions

1. Introduction

$\mathrm{Bi}_{1-x}\mathrm{Sb}_x$ are semimetals, which form a continuous series of solid solutions while varying the antimony concentration x [1–5]. Optical and electronic properties of these materials depend on many factors, including antimony content, temperature and a substrate material used (due to the difference in the thermal expansion coefficients of $\mathrm{Bi}_{1-x}\mathrm{Sb}_x$ and the substrate). Such a system allows

not only the study of the fundamental physical phenomena, but also use in many applications, such as thermoelectric, electronic and optical devices. The properties of thin films strongly differ from these of bulk media and are of great research interest [6,7]. At the temperature of 290 K, the influence of a size effect is minimal: the limitation of a mean free path is associated with the concentration of charge carriers. Many studies are dedicated to investigation of dependency of $Bi_{1-x}Sb_x$ sheet DC conductivity on antimony content, film thickness, and temperature [1–5]. In two recent works it was shown that thin bismuth-antimony films have tunable optical response in the THz frequency range [8,9]. In the work of Katayama et al., the optical response of charge carriers was investigated in thin films of Bi and $Bi_{1-x}Sb_x$ (x from 0 to 16 %) in a frequency range up to 50 THz, but the measurements were performed only for film thickness of 40 nm [8]. In the mentioned work, the dependencies of dynamical sheet resistivity (or conductivity) on antimony content and a frequency of THz radiation were not calculated, but it should be mentioned that a semiconducting Si(111) substrate used strongly affects these parameters. Using the Drude analysis, the authors have extracted the dependencies of the plasma frequency and damping rate of charge carriers on antimony concentration. They have also extracted the carrier density assuming that effective carrier mass (measured for bulk crystal at the helium temperature, but applied for thin film at the room temperature) depends on neither film thickness nor antimony concentration. However, the film thickness, temperature and a substrate material strongly affect this parameter [10,11]. To obtain the correct values of the mentioned parameters, it is necessary to use a dielectric substrate which has low losses in the THz frequency range.

In this work, we study the influence of thickness and antimony content x of thin-film $Bi_{1-x}Sb_x$ solid solutions as well as substrate material on their dynamical THz conductivity and galvanomagnetic properties at room temperature. From THz measurements, we extract the plasma frequency, relaxation time, DC conductivity and effective carrier mass and compare the obtained values with the results of galvanomagnetic measurements. These dependencies are important for application in simulation of various thermoelectric, electronic and optical devices, such as detectors of THz radiation or components which can control the properties of radiation in the THz frequency range, i.e., filters, modulators, phase and polarization shifters, etc. [12–16].

2. Materials and Methods

2.1. Synthesis

The thermal spraying method was used to obtain thin $Bi_{1-x}Sb_x$ films on mica and polyimide (PI) substrates. This method consists of evaporating the substance located on the evaporator and then condensing the substance on the substrate. To obtain a film from a bismuth-antimony solid solution, it is necessary to use the discrete evaporation method. The substance was poured into the evaporator in portions, thereby making it possible to obtain a film of uniform composition. The film was formed in vacuum at a pressure of 10^{-5} Torr, then the substance was deposited on a substrate (the temperature of the substrate was maintained equal to 120 °C). The annealing was performed at a temperature of 250 °C for 30 min. The film thicknesses were measured using Linnik's interferometry. The thickness measurement error is less than 5 nm. If the film thickness differed from the specified one by more than 5 nm, it was replaced with another one with the correct thickness. The chemical composition (antimony content) of the film was studied by X-ray fluorescence analysis with an accuracy of 0.05%.

2.2. X-ray Diffraction and Atomic Force Microscopy

The X-ray diffraction (XRD) measurements were performed for mica substrate, bulk Bi(111) single-crystal and a thin-film Bi and $Bi_{88}Sb_{12}$ (deposited on mica substrate) to evaluate the crystallographic orientation of a film (see Figure 1b). The observed bifurcated peak at 152.3 degrees (for Bi film) indicates the crystallographic plane (111). With adding antimony and increase of its concentration, the 5th order peak at 152.3 degrees for pure bismuth shifts to 157.2 degrees for $Bi_{88}Sb_{12}$. This angle change also makes it possible to estimate the concentration of antimony in a solid solution.

The atomic force microscopy (AFM, Figure 1c) additionally allows estimation of the film quality: there can be seen the crystal growth figures with a triangular shape of the observed plane (111) of the hexagonal cell and crystallite boundaries. From the point of view of transport phenomena, such a film with crystallite boundaries is a quasi-monocrystal for charge carriers.
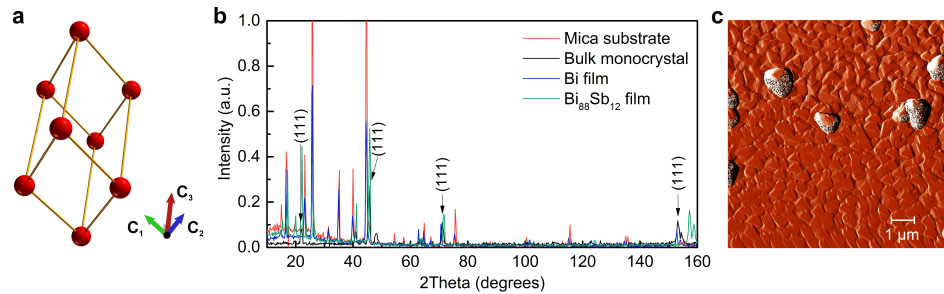
Figure 1. (**a**) Bismuth-like crystal structure. (**b**) X-ray diffraction patterns (Cu K-α emitter) for mica substrate, bulk Bi(111) monocrystal and a thin Bi and $Bi_{88}Sb_{12}$ films on substrate. (**c**) AFM image of a 150 nm film surface crystal (growth figures of a triangular shape and the observed (111) plane of the hexagonal cell).

2.3. Dual-Zone Model of Bismuth-Antimony

It is known that transport phenomena in bismuth and it compounds are anisotropic. Let us consider the limitations associated with anisotropy imposed on the transport coefficients by Onsager principle [17] and symmetry of the crystal. The trigonal axis (see Figure 1), is perpendicular to the film plane (z axis), and x axis is considered to coincide with one of the binary axes. Thus, we obtain three tensors for the measured transport coefficients.

Tensor for the resistivity of a film is

$$\rho_{ik} = \begin{vmatrix} \rho_{11} & 0 & 0 \\ 0 & \rho_{22} & 0 \\ 0 & 0 & \rho_{33} \end{vmatrix}. \tag{1}$$

Tensor for the Hall coefficient of a film is

$$R_{ik,l} = \begin{array}{c|ccc} ik & {}^{l}1 & 2 & 3 \\ \hline 11 & 0 & 0 & 0 \\ 22 & 0 & 0 & 0 \\ 33 & 0 & 0 & 0 \\ 23 & R_{23,1} & 0 & 0 \\ 32 & -R_{23,1} & 0 & 0 \\ 31 & 0 & R_{31,2} & 0 \\ 13 & 0 & -R_{31,2} & 0 \\ 12 & 0 & 0 & R_{12,3} \\ 21 & 0 & 0 & -R_{12,3} \end{array}. \tag{2}$$

Forth-stage tensor for magnetoresistivity of a film is

$$\rho_{ik,lm} = \begin{array}{c|cccccc} {}^{ik} & {}^{lm}11 & 22 & 33 & 23(32) & 12(21) & 13(31) \\ \hline 11 & \rho_{11,11} & \rho_{11,22} & \rho_{11,33} & \rho_{11,23} & 0 & 0 \\ 22 & \rho_{11,22} & \rho_{11,11} & \rho_{11,33} & -\rho_{11,23} & 0 & 0 \\ 33 & \rho_{33,11} & \rho_{33,11} & \rho_{33,33} & 0 & 0 & 0 \\ 23(32) & \rho_{23,11} & -\rho_{23,11} & 0 & \rho_{23,23} & 0 & 0 \\ 12(21) & 0 & 0 & 0 & 0 & \rho_{23,23} & \rho_{23,11} \\ 13(31) & 0 & 0 & 0 & 0 & \rho_{23,23} & \frac{1}{2}(\rho_{11,11} - \rho_{11,22}) \end{array}. \tag{3}$$

By phenomenological theory and crystallographic Bi and $Bi_{1-x}Sb_x$ film orientation tensor components ρ_{ik}, $R_{ik,l}$, $\rho_{ik,lm}$ match to the experimentally measured resistivity, Hall coefficient and magnetoresistivity. The magnetic field induction vector is parallel to a film plane normal. The resistivity, Hall coefficient and magnetoresistivity were measured experimentally and correspond to elements of tensors in trigonal plane. In case when a vector of magnetic induction is normal to plane ($\mathbf{B} \| \mathbf{n}$) and direct current is flowing through the film plane, the measured components match with ρ_{11}, $R_{12,3}$, $\rho_{11,33}$. This approximation can be used for single-crystal and block films as anisotropy for carriers in plane is minimal either for crystals: $\rho_{11} \approx \rho_{22}$. The relations between the tensor for $\rho(B)$ and tensor for $\sigma(B)$ components of the films in equations have the following form:

$$\rho_{11} = \frac{1}{\sigma_{11}}, \tag{4}$$

$$R_{12,3} = -\frac{\sigma_{12,3}}{\sigma_{11}^2}, \tag{5}$$

$$\rho_{11,33} = -\frac{\sigma_{11,33}}{\sigma_{11}^2} - \frac{\sigma_{12,3}^2}{\sigma_{11}^3}. \tag{6}$$

At these conditions and in dual-zone approximation (electrons of L-extremum in conductance band and holes of T-extremum in valence band) the studied transport coefficients are related with concentration and mobility of carriers in the following way:

$$1/\rho_{11} = en\frac{1}{2}(u_1^- + u_2^-) + epu^+, \tag{7}$$

$$R_{12,3} = -ep^2[nu_1^-u_2^- - p(u^+)^2], \tag{8}$$

$$\rho_{11,33} = \frac{\Delta\rho}{B^2} = \rho_{11}^2[ep(u^+)^3 + \frac{1}{2}enu_1^-u_2^-(u_1^- + u_2^-)] - \frac{R_{12,3}^2}{\rho_{11}}. \tag{9}$$

Here $\rho = \rho_{11}$ is the resistivity, $R = R_{12,3}$ is the Hall coefficient, $\Delta\rho$ is the resistivity variation in magnetic field, B is the magnetic field induction, u_1^-, u_2^-, u^+ are electron and hole mobilities in trigonal plane, n, p are electron and hole concentrations, e is the electron charge.

2.4. Terahertz Time-Domain Spectroscopy

The THz waveforms transmitted through the air, the substrate (reference signals) and the sample were obtained using terahertz time-domain spectroscopy (THz-TDS) setup. This setup is based on the application of an infrared femtosecond laser (1040 nm, 200 fs, 70 MHz, 15 nJ). The laser radiation is divided into pump and probe beams. The first one passes through the delay line and is used to excite the InAs semiconductor emitter which generates THz waves in the frequency range of 0.2–0.8 THz. After that, THz wave passes through the sample, while the infrared beam reflected from InAs is filtered. The first beam reaches the CdTe semiconductor detector where it meets the probe beam. The probe beam polarization in CdTe nonlinear crystal changes proportionally to the THz wave amplitude at a

given time point which depends on the time delay line position. Thus, the THz waveform is obtained by detecting the orthogonally polarized components difference of the probe beam (divided by a Wollaston prism) using a balanced photodetector. The measurements were performed at a temperature of 290 K. The complex amplitudes (amplitudes and phases) spectra were extracted by fast Fourier transform method. The complex sheet conductivity of thin film was calculated as [18]

$$\hat{\sigma}(f) = [(\hat{n}_{sub}(f) + 1)\hat{E}_{sub}(f)/\hat{E}_{sam}(f) - \hat{n}_{sub}(f) - 1]/Z_0, \tag{10}$$

where f is the frequency of THz radiation, Z_0 is the free space impedance, $\hat{E}_{sub}$ and $\hat{E}_{sam}$ are the complex amplitudes of THz wave transmitted through the substrate and the sample, and $\hat{n}_{sub}$ is the substrate complex refractive index which is calculated as

$$\hat{n}_{sub}(f) = c[\phi_{sub}(f) - \phi_{air}(f)]/(2\pi f d_{sub}) + 1 - i\,c\,ln(|\hat{E}_{sub}(f)|^2/|\hat{E}_{air}(f)|^2)/(4\pi f d_{sub}), \tag{11}$$

where c is the speed of light, ϕ_{sub} and ϕ_{air} are the phases of substrate and air signals, d_{sub} is the substrate thickness, i is the imaginary unit, $\hat{E}_{air}$ is the complex amplitude of THz wave transmitted through the air.

The complex permittivity of thin film can be extracted from the complex conductivity in the next form [19]:

$$\hat{\varepsilon}(f) = 1 + i\hat{\sigma}(f)/(2\pi f d_{film}\varepsilon_0), \tag{12}$$

where d_{film} is the film thickness (measured by Linnik interferometer) and ε_0 is the permittivity of free space.

3. Results and Discussion

3.1. Resistivity, Magnetoresistivity, and Hall Coefficient

Measurements of resistivity, magnetoresistivity and Hall coefficient were carried out in the magnetic field of 0.65 T.

As shown in Figure 2, at the temperature of 290 K the resistivity increases at increasing of Sb concentration and has higher value for thinner film. The character of the magnetoresistivity dependence on Sb content is opposite. A small value of magnetoresistivity shows that the main factor limiting charge carriers is their concentration. The studied film thicknesses are away from quantum oscillations range of thicknesses. Hence, in stationary conditions, we can assume the carrier concentration is the same for all the films from 70 to 150 nm for one composition. Figure 2c shows that for most of the films the Hall coefficient is negative and depends on external factors insignificantly. Negative sign of Hall coefficient shows that electron mobility is higher than hole one. It seems that dependency of Hall coefficient on Sb content is rather complex, and such behavior is due to variation of $Bi_{1-x}Sb_x$ band structure. The first calculation of thin-film bismuth-antimony band structure was performed in work of Suslov et al. for different film thicknesses using dual-zone model [11].

Mobility and concentration of electrons and holes in the trigonal plane (the film plane) were calculated using Equations (7)–(9). Calculation takes into account that solid solutions of bismuth-antimony are intrinsic semimetals which means that they have equal concentrations of electrons and holes. Mobility ratios for electrons (u_1^-, u_2^-) were taken from bulk crystal analysis. It allows a reduction of unknown values to three of them, which makes the Gauss method applicable for solving the equation system in stationary case.

Figure 2 shows the mobility and concentration of electrons and holes. The graph shows that the dependence of carrier concentration has a minimum at 5 at. %. The mobility of charge carriers weakly depends on the concentration of Sb, since the scattering of carriers occurs on themselves. For 150 nm film on mica, the electron and hole mobilities are both higher in the case of 3 % Sb. Thus, the value of Hall coefficient at this Sb content demonstrates that the hole conductivity makes the main contribution.
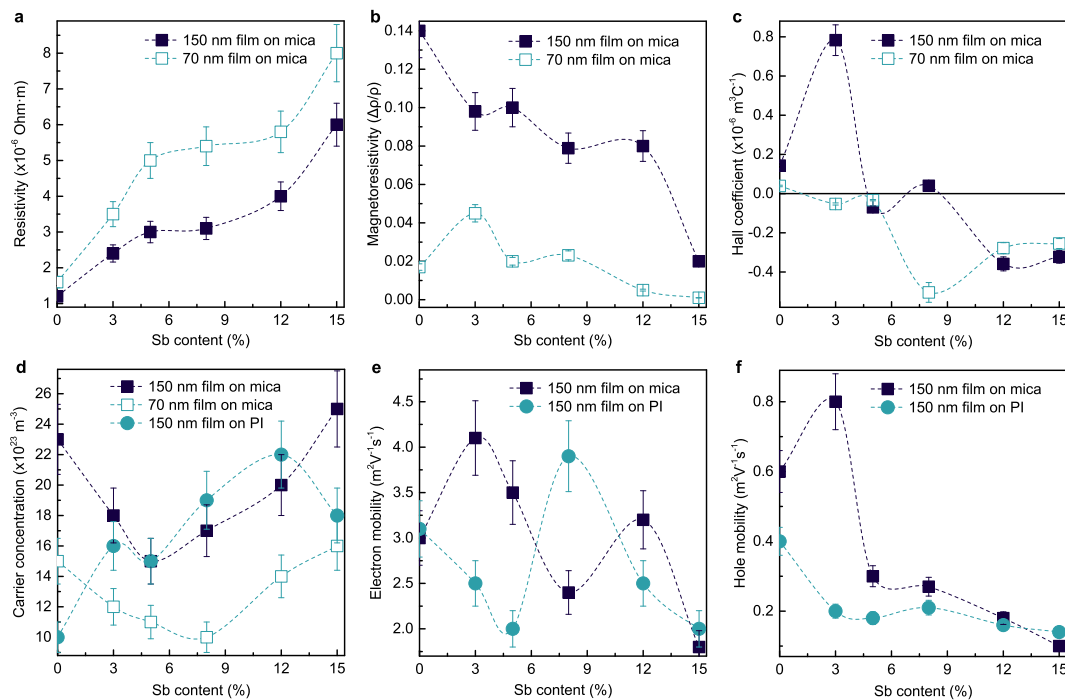
Figure 2. The dependencies of $Bi_{1-x}Sb_x$ sheet resistivity (**a**), magnetoresistivity (**b**) and Hall coefficient (**c**) on Sb concentration x for 150 nm and 70 nm films on mica substrate. (**d**) The same for carrier concentration in 150 nm films on mica and PI substrates and for 70 nm film on mica substrate. (**e**,**f**) The same for electron and hole mobility in 150 nm $Bi_{1-x}Sb_x$ films on PI and mica substrates.

3.2. THz Conductivity and Permittivity

The THz waveforms were measured for $Bi_{1-x}Sb_x$ solid solutions with Bi concentration x of 5, 8, 12 and 15 % and thickness of 150 nm and 70 nm, which were placed on the surface of mica (21 μm) and polyimide (42 μm) substrates (see Figure 3). The corresponding amplitude spectra are also shown in this Figure for 0.2–0.8 THz frequency range. Using Equations. (10)–(12), the film conductivity and permittivity dispersions (Figure 4 and 5) were extracted from the measured data.

As seen in Figure 3 both mica and PI substrates almost do not absorb the THz radiation (the decrease in transmittance is associated with Fresnel losses). On the contrary, the substrate/film structures transmit relatively small part of the radiation. This is due to both high reflectance of $Bi_{1-x}Sb_x$ films which are placed on the top side of the substrate and to high absorption in these semimetallic films. The transmittance is higher for the thinner films and is also slightly higher for the case of PI substrate. The latter effect is due to the lower conductivity of the films on PI substrate, as it will be shown below. It should be mentioned that the used substrate strongly affects the morphology of $Bi_{1-x}Sb_x$ polycrystalline films due to the morphology of a substrate surface (mica is a crystal, but PI is a polymer) and the difference between the thermal expansion coefficients of a substrate and a film. This difference plays an important role because such films are produced by thermal spraying method and are deformed in a cooling process. The substrate morphology affects the characteristic size of the crystallites, which makes the main contribution to a scattering of charge carriers and reduction of conductivity. The change of amplitude is more noticeable for the thinner films (70 nm) and is also higher in case of PI substrate.
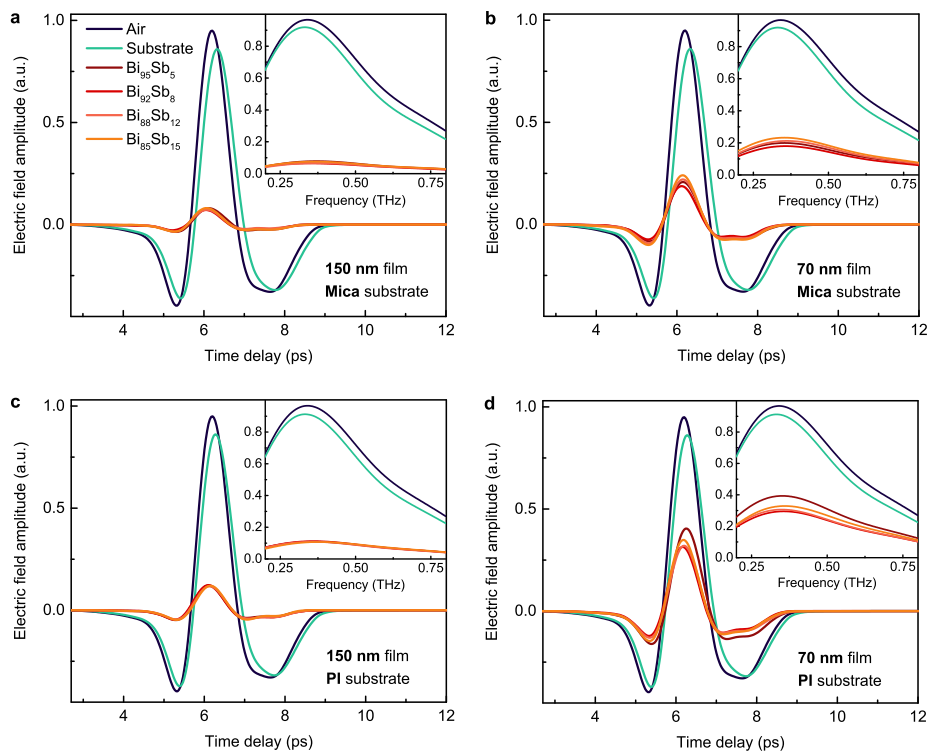
Figure 3. The temporary dependencies of a relative electric field amplitude of THz wave (THz waveforms) transmitted through the air, mica (**a**,**b**) and PI (**c**,**d**) substrates and full substrate/film structures for film thicknesses of 150 nm (**a**,**c**) and 70 nm (**b**,**d**) and in cases of various Sb concentrations. The corresponding amplitude spectra are shown in the insets for 0.2–0.8 THz frequency range.
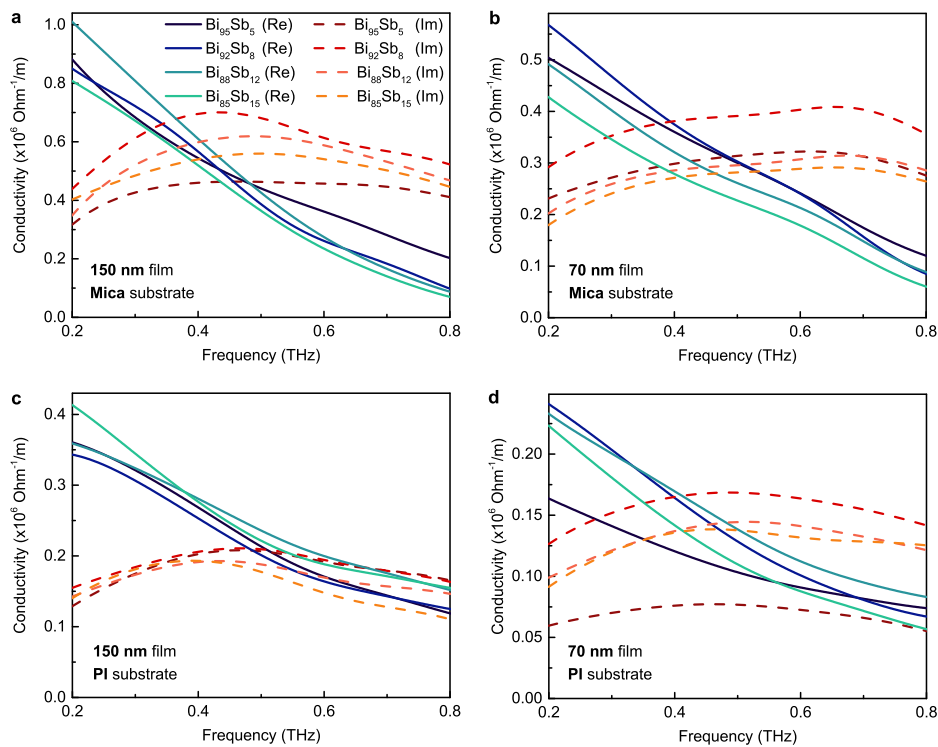
Figure 4. The dynamical complex conductivity spectra of $Bi_{1-x}Sb_x$ films in 0.2–0.8 THz frequency range for the cases of mica (**a**,**b**) and PI (**c**,**d**) substrates and for 150 nm (**a**,**c**) and 70 nm (**b**,**d**) film thicknesses. Different colors represent different Sb concentrations. The solid and dashed lines represent the real and imaginary parts of conductivity, respectively.

As shown in Figure 4 the conductivity is higher in case of thicker films and for mica substrate usage (due to a lower scattering rate of charge carriers). However, both real and imaginary parts of conductivity show better tunability (when varying the Sb concentration) in case of thinner samples (for 70 nm films). With the THz signal frequency increasing, the real part of film conductivity tends to decrease for all presented cases, while the imaginary part has a certain maximum value. This behavior is in a good agreement with a classical Drude model for charge carriers due to the semimetallic properties of the $Bi_{1-x}Sb_x$ films. It should be mentioned that the conductivity of these thin-film solid solutions non-linearly depends on the Sb concentration x due to the complex behavior of their band structure. The similar behavior of conductivity of such materials was reported in several works [1–3], where the DC measurements were performed.
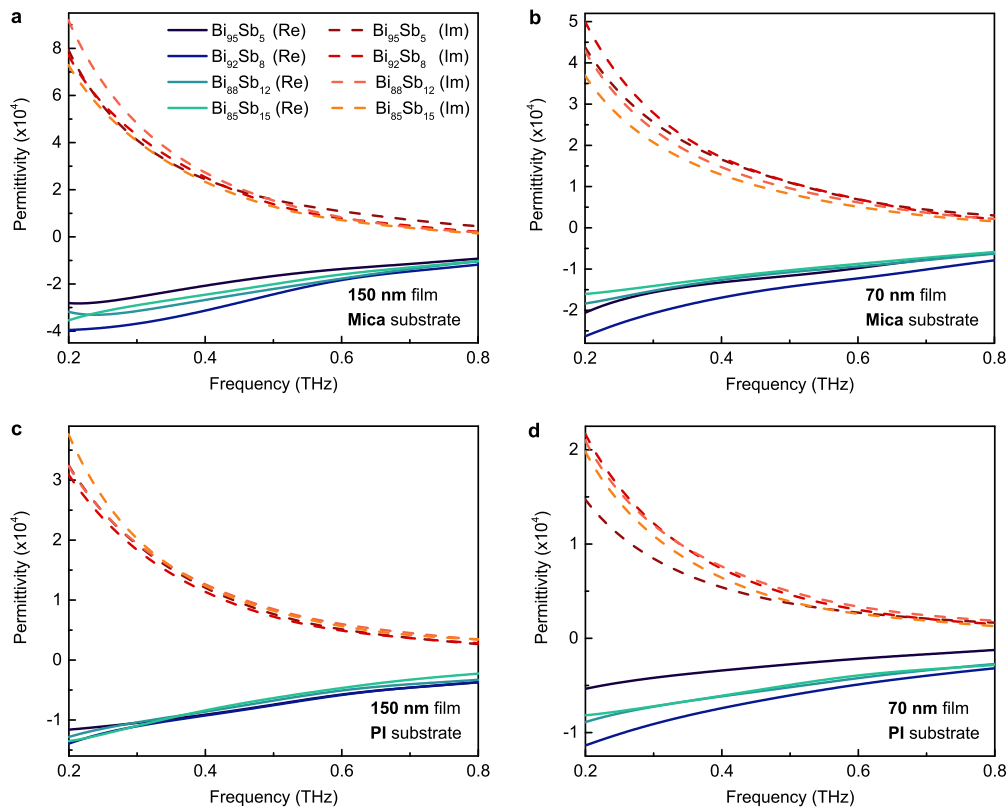
Figure 5. The dynamical complex permittivity spectra of $Bi_{1-x}Sb_x$ films in 0.2–0.8 THz frequency range for the cases of mica (**a**,**b**) and PI (**c**,**d**) substrates and for 150 nm (**a**,**c**) and 70 nm (**b**,**d**) film thicknesses. Different colors represent different Sb concentrations. The solid and dashed lines represent the real and imaginary parts of permittivity, respectively.

Based on Figure 5 it can be concluded that for complex permittivity spectra the similar behavior is observed as for complex sheet conductivity ones. In 0.2–0.8 THz frequency range, the real part of permittivity has very large negative values, which is also in a good enough agreement with the classical Drude model for metals/semimetals. This model was applied simultaneously to both conductivity and permittivity spectra (to increase the approximation accuracy) in the next form:

$$\hat{\sigma}(\omega) = \frac{\sigma_0}{1 - i\omega\tau} = \frac{\sigma_0}{1 + \omega^2\tau^2} + i\omega\tau\frac{\sigma_0}{1 + \omega^2\tau^2}, \tag{13}$$

$$\hat{\varepsilon}(\omega) = \varepsilon_\infty - \frac{\omega_p^2}{\omega^2 + i\gamma\omega}, \tag{14}$$

where $\omega = 2\pi f$ is the angular frequency of THz radiation, τ is the relaxation time of charge carriers which can be approximately estimated (using Equation (13) after splitting $\hat{\sigma}(\omega)$ into real and imaginary parts and their equalization through σ_0) as

$$\tau = \frac{1}{\omega} \frac{Im[\hat{\sigma}(\omega)]}{Re[\hat{\sigma}(\omega)]},$$
$$Re[\hat{\sigma}(\omega)] = \frac{\sigma_0}{1 + \omega^2 \tau^2},$$
$$Im[\hat{\sigma}(\omega)] = \omega\tau \frac{\sigma_0}{1 + \omega^2 \tau^2} \tag{15}$$

with small dispersion (τ can vary in process of THz wave transmission, because the THz pulse duration is about 10 times higher than the relaxation time value),

$$\sigma_0 = n(\omega)e^2\tau/m^* \tag{16}$$

is the DC film conductivity, where $n(\omega)$ is a concentration of the charge carriers (see below), e is the electron charge, m^* is the effective mass (the only one free fitting parameter), $\varepsilon_\infty = 100$ (high-frequency dielectric constant) for all the films, $\gamma = 1/\tau$ is the damping rate,

$$\omega_p^2 = ne^2/(\varepsilon_0 m^*) \tag{17}$$

is the square of plasma frequency, ε_0 is the permittivity of free space. Due to the fact that the film is irradiated with a THz wave, the additional charge carriers are generated besides the static carrier concentration:

$$n(\omega) = n_0 + \frac{[1 - R(\omega)]\alpha(\omega)W(\omega) \cdot C}{\hbar\omega}, \tag{18}$$

where n_0 is the carrier concentration without the external influence (obtained from galvanomagnetic measurements), $R(\omega)$ is the film reflection coefficient (estimated using the Fresnel equation for a normal irradiation from Equations (11) and (12)), $\alpha(\omega)$ is the absorption constant (from a complex refractive index, root of Equation (12)), $W(\omega)$ is the intensity spectrum of THz emitter which is normalized through the introduction of some constant value C, and $\hbar\omega$ is the photon energy. Thus, the complete Drude model was used to fit both experimental conductivity and permittivity data. This model takes into account the complex dependency of carrier concentration on THz field intensity in semimetallic $Bi_{1-x}Sb_x$ films. The results of data fitting are presented in Figure 6 for various Sb concentrations x (plasma frequency and relaxation time, DC conductivity and effective carrier masses).

As seen in Figure 6 the film thickness and the substrate material strongly affect the values of all the presented parameters. The nonlinear behavior of the curves is defined by a complex dependency of $Bi_{1-x}Sb_x$ band structure on antimony concentration x. The DC conductivity is higher for films on mica substrate due to a higher relaxation time (lower damping rate, associated with a greater crystallite size). However, it has more stable behavior in case of PI substrate due to low difference of film and PI thermal expansion coefficients. The plasma frequency and effective carrier mass (averaged effective mass of electrons and holes) curves have opposite dependencies and are smoother than DC conductivity curves. The 150 nm films on mica have the lower carrier effective mass (higher quality) over all the studied samples. The 70 nm films on mica have a higher value of this parameter due to their lower thicknesses (carrier scattering). The 150 nm and 70 nm films on PI have similar dependencies, but their values are both higher (due to lower quality, smaller crystallites) than in case of mica substrate. The reason for the presented behavior of the relaxation times with antimony variation can be associated with many factors that lead to changes in the band structure of the material. The relaxation times are obtained based on the Drude analysis, so it is difficult to separate the contributions from the substrate used, crystallite size, film thickness, etc.
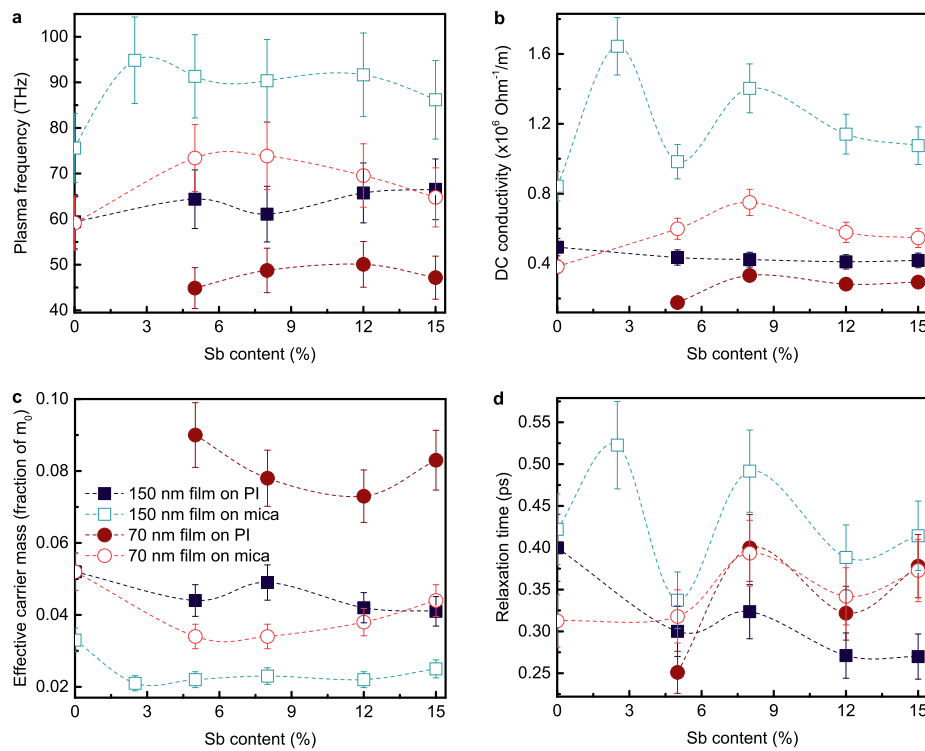
Figure 6. Parameters extracted using Drude model for conductivity/permittivity in cases of various Sb concentrations: plasma frequency (**a**) and relaxation time (**d**), DC conductivity (**b**) and effective carrier masses (**c**) in fraction of m_0. The points for 0 % antimony concentration (pure bismuth) and for 150 nm $Bi_{97.5}Sb_{2.5}$ (on mica substrate) are added based on another THz measurements of thin Bi films with various thicknesses.

Figure 7 shows the DC conductivity of 150 nm and 70 nm $Bi_{1-x}Sb_x$ films (on mica substrate) obtained by resistivity measurements in direct current and extracted from dynamical THz conductivity using Drude model approximation.
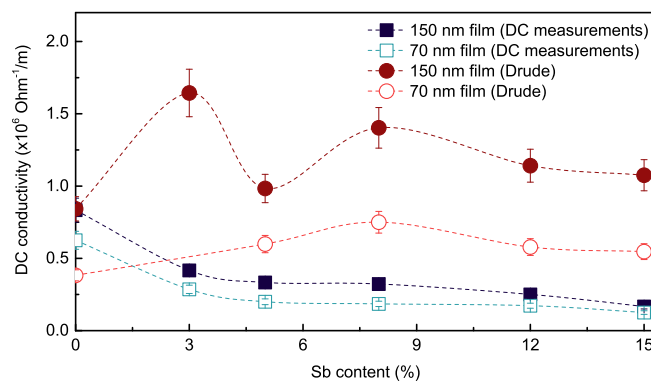
Figure 7. Comparison of DC conductivity for 150 nm and 70 nm $Bi_{1-x}Sb_x$ films (on mica substrate) directly measured in DC configuration and extracted from THz measurements using Drude model.

The relation of values between two different thicknesses for two mentioned methods are similar, but the DC conductivity extracted from THz spectroscopy experiment is higher due to the THz field-induced additional charge carriers in thin films (according to Equation (18)). The increment of effective DC conductivity is higher for thicker film due to a higher absorption.

4. Conclusions

The galvanomagnetic and terahertz spectroscopy measurements were performed for semimetallic $Bi_{1-x}Sb_x$ thin films with various antimony concentrations x and thicknesses which were placed on the surface of polyimide and mica substrates. It was shown that film static and dynamic resistivity (conductivity) as well as dielectric permittivity depends on Sb content and the film thickness. The substrate material also influences on these parameters due to the difference in thermal expansion coefficients of a film and a substrate and due to the substrate type: crystal or polymer. The Drude analysis was applied to the measured dispersions: the plasma frequency and relaxation time as well as effective carrier mass were extracted. It was shown that carrier concentration almost does not depend on any of the mentioned parameters at room temperature. The carrier effective mass and mobility strongly depend on film thickness and the substrate material. The measurements were performed at room temperature that opens the possibility to use the obtained dispersions in analytical and electromagnetic simulations of various thermoelectric, electronic and optical devices which work at normal conditions, such as detectors of THz radiation or components which can control the properties of radiation in the THz frequency range, i.e., filters, modulators, phase and polarization shifters, and many others.

Conflicts of Interest: The authors declare no conflict of interest. The funders had no role in the design of the study; in the collection, analyses, or interpretation of data; in the writing of the manuscript, or in the decision to publish the results.

References

1. Dutta, S.; Shubha, V.; Ramesh, T.; D'sa, F. Thermal and electronic properties of $Bi_{1-x}Sb_x$ alloys. *J. Alloy. Compd.* **2009**, *467*, 305–309. [CrossRef]
2. Lenoir, B.; Cassart, M.; Michenaud, J.P.; Scherrer, H.; Scherrer, S. Transport properties of Bi-rich Bi-Sb alloys. *J. Phys. Chem. Solids* **1996**, *57*, 89–99. [CrossRef]
3. Cho, S.; DiVenere, A.; Wong, G.K.; Ketterson, J.B.; Meyer, J.R. Transport properties of $Bi_{1-x}Sb_x$ alloy thin films grown on CdTe (111) B. *Phys. Rev. B* **1999**, *59*, 10691. [CrossRef]
4. Lenoir, B.; Dauscher, A.; Cassart, M.; Ravich, Y.I.; Scherrer, H. Effect of antimony content on the thermoelectric figure of merit of $Bi_{1-x}Sb_x$ alloys. *J. Phys. Chem. Solids* **1998**, *59*, 129–134. [CrossRef]
5. Malik, K.; Das, D.; Mondal, D.; Chattopadhyay, D.; Deb, A.; Bandyopadhyay, S.; Banerjee, A. Sb concentration dependent structural and resistive properties of polycrystalline Bi-Sb alloys. *J. Appl. Phys.* **2012**, *112*, 083706. [CrossRef]
6. Ohring, M. *Materials Science of Thin Films*; Elsevier: Amsterdam, The Netherlands, 2001.
7. Aspnes, D.E. Optical properties of thin films. *Thin Solid Films* **1982**, *89*, 249–262. [CrossRef]
8. Katayama, I.; Kawakami, H.; Hagiwara, T.; Arashida, Y.; Minami, Y.; Nien, L.W.; Handegard, O.; Nagao, T.; Kitajima, M.; Takeda, J. Terahertz-field-induced carrier generation in $Bi_{1-x}Sb_x$ Dirac electron systems. *Phys. Rev. B* **2018**, *98*, 214302. [CrossRef]
9. Li, X.; Yoshioka, K.; Xie, M.; G Timothy Noe, I.; Lee, W.; Peraca, N.M.; Gao, W.; Hagiwara, T.; Handegård, Ø.S.; Nien, L.W.; et al. Terahertz Faraday and Kerr rotation spectroscopy of $Bi_{1-x}Sb_x$ films in high magnetic fields up to 30 tesla. *Phys. Rev. B* **2019**, *100*, 115145. [CrossRef]
10. Komarov, V.; Suslov, A.; Suslov, M. Galvanomagnetic properties of $Bi_{85}Sb_{15}$ thin films on different substrates. *Semiconductors* **2017**, *51*, 702–705. [CrossRef]
11. Suslov, A.; Grabov, V.; Komarov, V.; Demidov, E.; Senkevich, S.; Suslov, M. The Band-Structure Parameters of $Bi_{1-x}Sb_x$ ($0 \leq x \leq 0.15$) Thin Films on Substrates with Different Thermal-Expansion Coefficients. *Semiconductors* **2019**, *53*, 611–614. [CrossRef]

12. Tang, W.; Politano, A.; Guo, C.; Guo, W.; Liu, C.; Wang, L.; Chen, X.; Lu, W. Ultrasensitive Room-Temperature Terahertz Direct Detection Based on a Bismuth Selenide Topological Insulator. *Adv. Funct. Mater.* **2018**, *28*, 1801786. [CrossRef]

13. Wei, Z.; Li, X.; Yin, J.; Huang, R.; Liu, Y.; Wang, W.; Liu, H.; Meng, H.; Liang, R. Active plasmonic band-stop filters based on graphene metamaterial at THz wavelengths. *Opt. Express* **2016**, *24*, 14344–14351. [CrossRef] [PubMed]

14. Grebenchukov, A.N.; Zaitsev, A.D.; Novoselov, M.G.; Kornilov, E.V.; Khodzitsky, M.K. Optically tunable Fano-resonant filter based on graphene. In *Metamaterials, Metadevices, and Metasystems 2017*; International Society for Optics and Photonics: San Diego, CA, USA, 2017; Volume 10343, p. 103432V.

15. Grebenchukov, A.; Azbite, S.; Zaitsev, A.; Khodzitsky, M. Faraday effect control in graphene-dielectric structure by optical pumping. *J. Magn. Magn. Mater.* **2019**, *472*, 25–28. [CrossRef]

16. Masyukov, M.; Vozianova, A.; Grebenchukov, A.; Gubaidullina, K.; Zaitsev, A.; Khodzitsky, M. Optically tunable terahertz chiral metasurface based on multi-layered graphene. *Sci. Rep.* **2020**, *10*, 1–10. [CrossRef] [PubMed]

17. Onsager, L. Reciprocal Relations in Irreversible Processes. I. *Phys. Rev.* **1931**, *37*, 405–426. [CrossRef]

18. Tinkham, M. Energy gap interpretation of experiments on infrared transmission through superconducting films. *Phys. Rev.* **1956**, *104*, 845. [CrossRef]

19. Novotny, L.; Hecht, B. *Principles of Nano-Optics*; Cambridge University Press: Cambridge, UK, 2012.